nanomaterials

MDPI

Article

Efficient Photoelectrochemical Water Splitting by Tailoring MoS_2/CoTe Heterojunction in a Photoelectrochemical Cell

Effat Sitara, Habib Nasir *, Asad Mumtaz, Muhammad Fahad Ehsan, Manzar Sohail, Sadia Iram and Syeda Aqsa Batool Bukhari

School of Natural Sciences, National University of Sciences and Technology, H-12, Islamabad 44000, Pakistan; effat.sitara@sns.nust.edu.pk (E.S.); asad.mumtaz@sns.nust.edu.pk (A.M.); m.fahad.ehsan@sns.nust.edu.pk (M.F.E.); manzar.sohail@sns.nust.edu.pk (M.S.); sadia.iram@sns.nust.edu.pk (S.I.); aqsa.batool@sns.nust.edu.pk (S.A.B.B.)

* Correspondence: habibnasir@sns.nust.edu.pk

Received: 14 October 2020; Accepted: 30 October 2020; Published: 26 November 2020

Abstract: Solar energy conversion through photoelectrochemical water splitting (PEC) is an upcoming promising technique. MoS_2/CoTe heterostructures were successfully prepared and utilized for PEC studies. MoS_2 and CoTe were prepared by a hydrothermal method which were then ultrasonicated with wt. % ratios of 1:3, 1:1 and 3:1 to prepare MoS_2/CoTe (1:3), MoS_2/CoTe (1:1) and MoS_2/CoTe (3:1) heterostructure, respectively. The pure materials and heterostructures were characterized by XRD, UV–vis-DRS, SEM, XPS, PL and Raman spectroscopy. Photoelectrochemical measurements were carried out by linear sweep voltammetry and electrochemical impedance spectroscopic measurements. A maximum photocurrent density of 2.791 mA/cm^2 was observed for the MoS_2/CoTe (1:1) heterojunction which is about 11 times higher than the pristine MoS_2. This current density was obtained at an applied bias of 0.62 V vs. Ag/AgCl (1.23 V vs. RHE) under the light intensity of 100 mW/cm^2 of AM 1.5G illumination. The enhanced photocurrent density may be attributed to the efficient electron–hole pair separation. The solar to hydrogen conversion efficiency was found to be 0.84% for 1:1 MoS_2/CoTe, signifying the efficient formation of the p-n junction. This study offers a novel heterojunction photocatalyst, for PEC water splitting.

Keywords: photoelectrochemical water splitting; heterojunction; molybdenum disulfide; cobalt telluride

1. Introduction

The sun is a huge source of energy. It is important to explore new ways of utilizing solar energy so that the problem of energy crises and global warming through environmental emission of gasses can be addressed [1]. Using solar energy to convert water into oxygen and hydrogen is a promising approach to remove energy shortages and environmental pollution [2]. Water splitting through a photoelectrochemical method has drawn tremendous attention because it is pollution and carbon-free technology [3,4]. The goal of clean energy can be achieved by the formation of heterostructures, thereby engineering the surface of the semiconductors [5,6]. One way to produce an effective photocatalyst is to use the p-n junction as a photoanode in the photoelectrochemical devices [7,8]. This p-n junction provides a medium or space-charge region where electrons from the n-type semiconductor and holes from the p-type semiconductor are mobilized [9]. This region launches an electrostatic field that helps to reduce the electron–hole recombination and enables easy transport of electrons [10].

Transition metal di-chalcogenides like molybdenum disulfide are being extensively studied now a days due to their excellent electrical [11–13], mechanical [14,15], photoelectrochemical [16,17], photocatalytic [18–20], optical [21,22], sensing [23–25] and photovoltaic [26–28] properties. MoS_2 is an n-type semiconductor having a direct bandgap of 1.9 eV. Few layer MoS_2 is considered to be a good photoanode for photoelectrochemical water splitting (PEC) due to its band gap in the solar absorption spectrum [29]. Its highly active edge sites display efficient photocatalytic activity [30]. To overcome the problem of recombination of electrons and holes, effective charge separation and charge transfer, various heterojunctions of MoS_2 with different materials are reported till now, including the latest as ZnO/MoS_2 [16], $p\text{-}GaN/MoS_2$ [31], $CdS@CoMo_2S_4/MoS_2$ [32], MnS/MoS_2 [33] for PEC water splitting. The thrust for a better material continues and new materials are being reported every hour. However, its composite with cobalt telluride is not yet reported, to the best of our knowledge.

Cobalt telluride is a p-type semiconductor having a band gap of 2.15 eV [34]. It has shown good photocatalytic activity for CO_2 reduction [35]. The composites of CoTe with Si-Microwires has also been used for solar water splitting [36]. Although, MoS_2 and CoTe both have comparable band gaps with their specific intrinsic properties but their unique combination to develop an effective p-n junction is not reported yet. This study aims to understand few important factors in this novel MoS_2/CoTe heterostructure which are, charge separation, electron–hole recombination, charge transfer and photoconversion efficiency for PEC water splitting. This novel heterojunction could be promising and is required to be explored in detail, under visible light irradiation for improved photoelectrochemical water splitting.

In this work, MoS_2/CoTe p-n heterojunction was fabricated by a simple sonochemical method. The as-prepared heterostructures showed a high photoelectrochemical response towards water splitting. The heterostructures showed much better activity than the pure counterparts, due to the successful creation of the p-n junction and effective separation of the conduction and valence bands, thereby reducing the electron–hole recombination.

2. Results and Discussion

2.1. Phase Analysis

X-ray diffraction studies were carried out to approve the crystallinity and structures of the prepared photocatalysts as shown in Figure 1a. CoTe showed diffraction peaks at 31.4°, 43°, 47.2°, 57.5°, 58.5° and 56.7° corresponding to the (101), (102), (110), (201), (112) and (201) hexagonal phases and match with the standard JCPDS card No. 00-034-0420 [35]. On the other hand, diffraction peaks at 14°, 28.7°, 34.4°, 42.6° and 57.5° correspond to the (002), (103), (100), (105) and (110) planes of the hexagonal wurtzite structure of MoS_2 [37] and match with the JCPDS card No. 37-1492 [38]. The exact matching of the peaks of CoTe and MoS_2 with the standards show that there is no impurity present in the sample. The composites of MoS_2 and CoTe with ratios of 1:3 MoS_2/CoTe (1:3 MC), 1:1 MoS_2/CoTe (1:1 MC) and 3:1 MoS_2/CoTe (3:1 MC) show good correspondence with the pure MoS_2 and CoTe. The peak intensity of the characteristic peak of MoS_2 at 14° decreases with increase in the ratio of CoTe, i.e., 3:1 MC > 1:1 MC > 1:3 MC in the heterostructures. The heterostructure 1:1 MC shows characteristic peaks from both MoS_2 and CoTe. This can be attributed to the successful formation of heterostructures.

2.2. Raman Analysis

To further understand the microstructure and the crystallinity of the photocatalysts, Raman spectra were taken as shown in Figure 1b. In Raman spectra of MoS_2, two peaks are very prominent at around 380 and 405 cm^{-1} which match the E^1_{2g} and A_{1g} in-plane vibration of Mo and S atoms and out of plane vibrations of sulfur atoms from pure 2H-MoS_2 [39], respectively. The difference between the peaks of E^1_{2g} and A_{1g} is 24 cm^{-1} which is comparable to previously reported four-layered MoS_2 [40]. However, CoTe did not show any peak. While the MoS_2/CoTe with different ratios shows the effect of compositional modifications while forming a heterojunction. The intensity of E^1_{2g} and A_{1g} peaks of

MoS_2 is being supported by increasing the composition of CoTe in the heterojunction. This illustrates the effective interfacial interaction between the individual components of the heterojunction required for the efficient charge transfer phenomenon during photocatalytic processes.

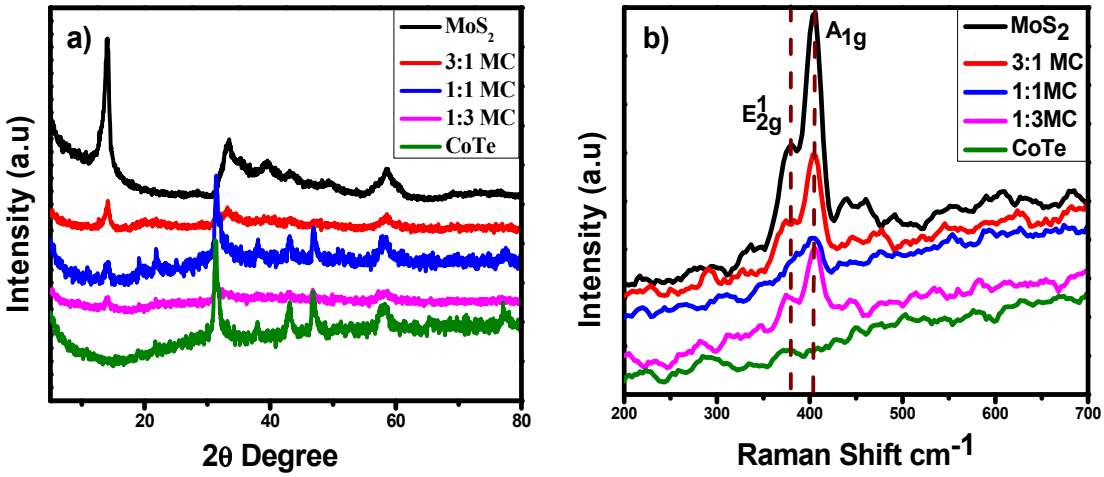

Figure 1. (**a**) X-ray diffraction pattern of CoTe, MoS_2, 1:3 MoS_2/CoTe (MC), 1:1 MC, 3:1 MC. (**b**) Raman shift values of MoS_2, CoTe and their composites.

2.3. Structural and Compositional Analysis

Morphology of the as-synthesized photocatalysts was studied through scanning electron microscopy (SEM) shown in Figure 2. The flower-like structure of MoS_2 is observed in Figure 2a, well-matched with the previously reported flowerlike nanosheets of MoS_2 [41]. While Figure 2b for 1:1 MC shows the successful decoration of CoTe nanostructures on the surface of the flower-like structure with highly porous features of MoS_2. The morphology shows the homogeneous mixing of two components in the heterojunction of 1:1 MC. This homogeneity with its effective interfacial contact developed by using the sonochemical method is beneficial in photocatalysis during the charge transfer phenomenon from CoTe to MoS_2. In Figure 2c, the pure CoTe showed a semicircular and agglomerated morphology mainly due to the magnetic properties of CoTe [36]. SEM images of 3:1 MC and 1:3 MC are shown in Figure S1.

Energy-dispersive X-ray spectroscopy (EDS) helps to find the purity and elemental composition of the prepared materials [42]. The EDS spectra in Figure 2d show the elemental composition of 1:1 MC. The peaks of Mo, S, Co and Te are clearly visible. The peaks for Si and O are due to the glass slides used for the sample preparation for SEM analysis. Figure S2a–d show there are no impurities found in the formation of pure materials and composites, which demonstrates the purity of the synthesized materials.

2.4. XPS Analysis

Oxidation states and chemical composition of the prepared materials were established by employing the X-ray photoelectron spectroscopy. XPS spectra of Mo3d and S2p are shown in Figure 3a,b. The Mo^{4+} oxidation state was confirmed by the binding energies for $Mo3d_{5/2}$ at 229.01 eV and $Mo3d_{3/2}$ at 232.24 eV [43]. The presence of sulfur can be established by the peak at 161.7 eV for $S2p_{3/2}$ orbital and 163.48 eV for $S2p_{1/2}$ [17]. The peaks positioned at 233.1 eV and 236.2 eV can be ascribed to the Mo^{+6} $3d_{5/2}$ and Mo^{+6} $3d_{3/2}$ oxidation state which appears due to minor oxidation of the edges during MoS_2 synthesis [44,45]. Figure 3c shows peaks at 781 eV and 796.8 eV for Co $2p_{3/2}$ and $2p_{1/2}$, respectively, which appear due to the existence of the Co^{2+} oxidation state [46]. The peaks appearing in Figure 3d at 573.2 eV and 583.6 eV correspond to the $Te3d_{5/2}$ and $Te3d_{3/2}$, respectively, which show the Co^{2+} oxidation state of tellurium in the CoTe [36]. The other peaks are credited to the

oxides of cobalt and tellurium which might be due to the reaction of the surface of CoTe with oxygen in the atmosphere [35].

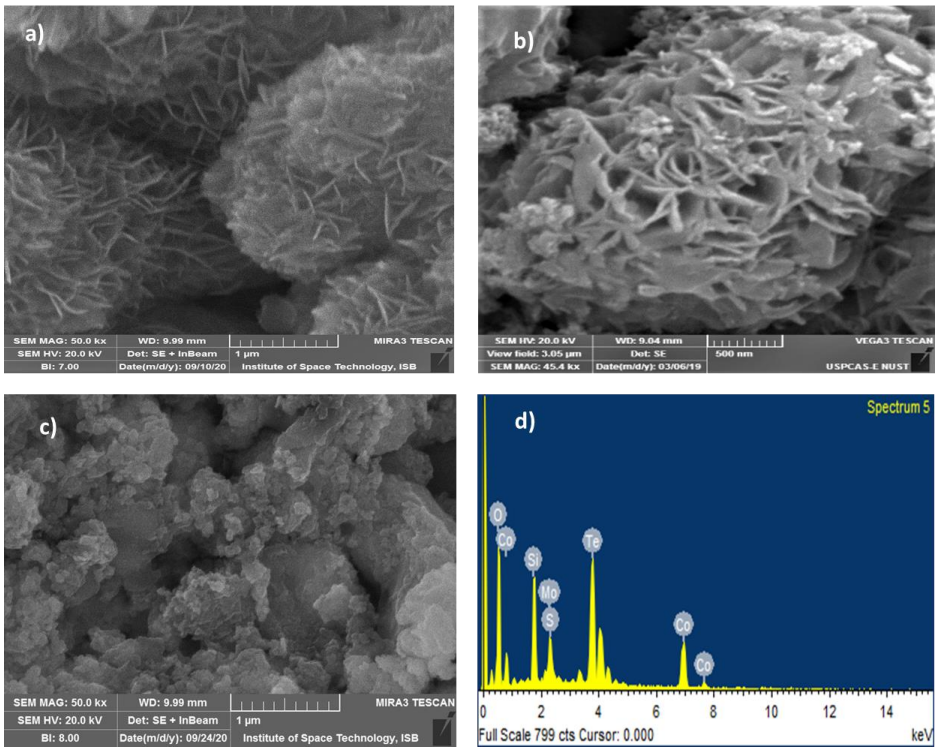

Figure 2. SEM images of (**a**) MoS_2 at 1 µm, (**b**) 1:1 MC at 500 nm, (**c**) CoTe at 1 µm, (**d**) EDS spectra of 1:1 MC.

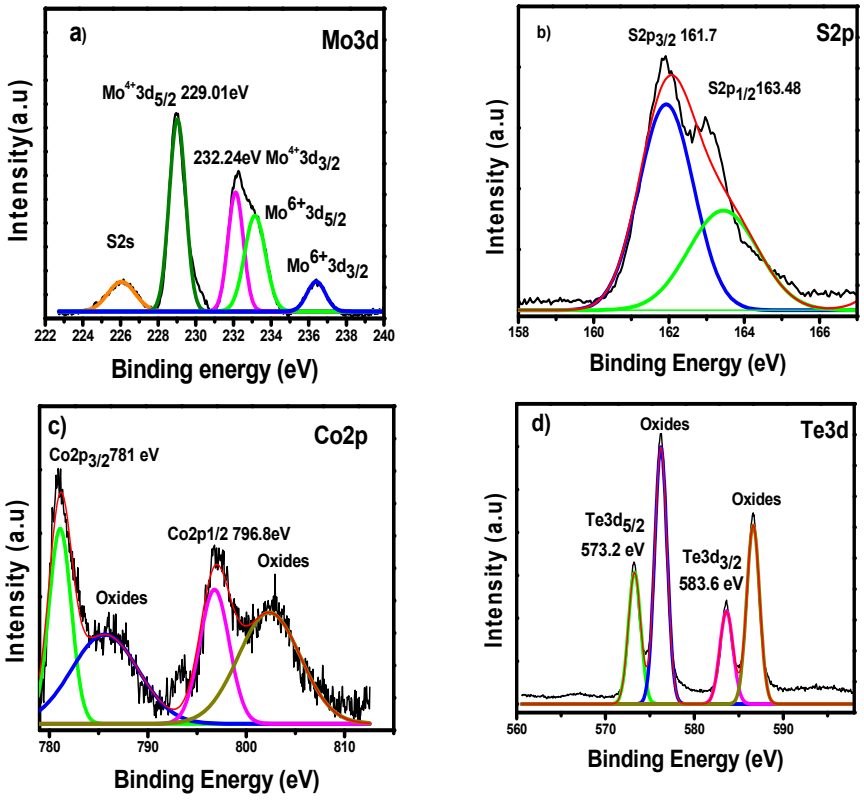

Figure 3. XPS spectra of MoS_2 (**a**) Mo3d, (**b**) S2p and CoTe (**c**) Co2p, (**d**) Te3d.

2.5. Alignment of Energy Levels

The main features for the understanding of the mechanism of a photoelectrochemical process are the position of the valence and conduction bands and band gap against the standard hydrogen electrode (SHE) and they help to align the energy levels [47].

UV-Vis diffused reflectance spectra(DRS) were obtained to evaluate the optical properties of the synthesized materials. Kubelka–Munk equation was employed to calculate the band gap by converting the diffused reflectance calculation to equivalent absorption coefficients of both MoS_2 and CoTe. Tauc plots were plotted to calculate the band gap shown in Figure 4a. MoS_2 came out with a band gap of 1.73 eV and CoTe with 2.24 eV as shown in Figure 4b.

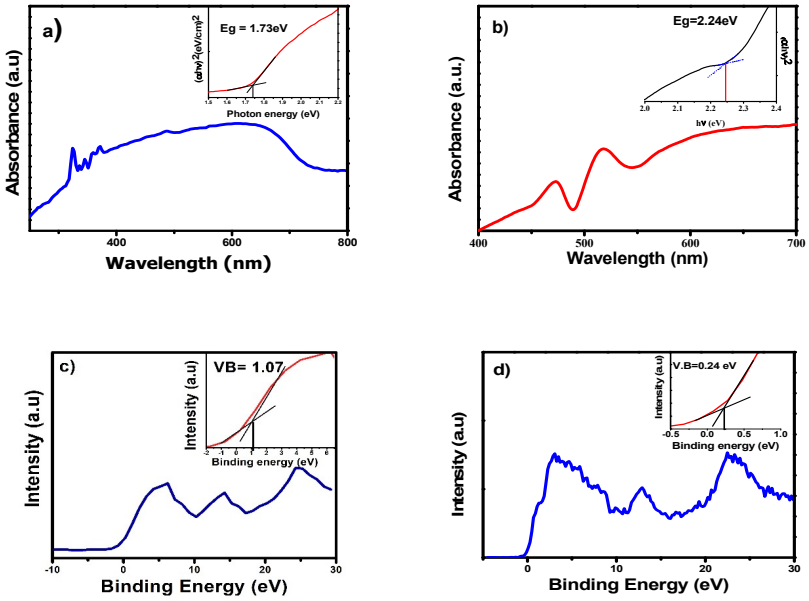

Figure 4. UV–vis-DRS spectrum of (**a**) MoS_2, (**b**) CoTe with insets showing the respective Tauc plots and band gap of MoS_2 and CoTe. (**c**) MoS_2 and (**d**) CoTe are the XPS spectra for valence band positions in the corresponding insets.

The XPS spectra for valence band show a valence band position for MoS_2 in Figure 4c to be 1.07 eV and it shows the valence band position for CoTe as 0.24 eV in Figure 4d. The energy levels are aligned and drawn in accordance with these readings. The alignment of energy levels is shown in Figure 5.

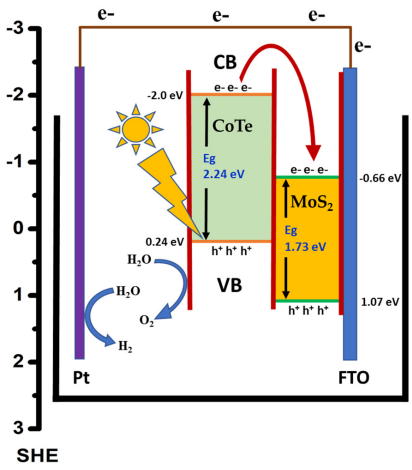

Figure 5. Schematic illustration of alignment of the energy level of MoS_2/CoTe nanocomposite showing photoelectrochemical water splitting.

2.6. Photoelectrochemical Analysis

To examine the photoelectrochemical activity of the photocatalysts, linear sweep voltammograms were collected under illumination as shown in Figure 6. Pristine MoS_2 and CoTe showed a photocurrent density of 0.26 mA/cm^2 and 0.59 mA/cm^2 at 0.62 V vs. Ag/AgCl (1.23 V vs. RHE) under visible light illumination of 100 mW/cm^2 with AM 1.5 G, respectively. The photocurrent densities of MoS_2/CoTe with 1:3 MC, 1:1 MC and 3:1 MC are found to be 0.97, 2.79 and 1.59 mA/cm^2 at 1.23 V vs. RHE under visible light illumination intensity of 100 mW/cm^2 are observed, respectively. Figure 6a shows the gradual increase in the photocurrent response in the form of a bump in peak for the 1:1 ratio of photocatalyst around the voltage of 0.24 V. This reveals that the photoexcited charges have moved from the valance band to the conduction band and a point of saturation is attained due to the maximum electron movement to the conduction band and fulfillment of the active sites on the surface of the photocatalyst. A maximum photocurrent density was observed in MoS_2/CoTe with a 1:1 ratio which is 11 times higher than pristine MoS_2 and four times greater than pristine CoTe. It is observed that Ohmic J-V curves originate in individual components of the heterojunction while MoS_2/CoTe with a 1:1 ratio shows a standard peak of photoelectrochemical water splitting with its maximum saturation potential stabilization.

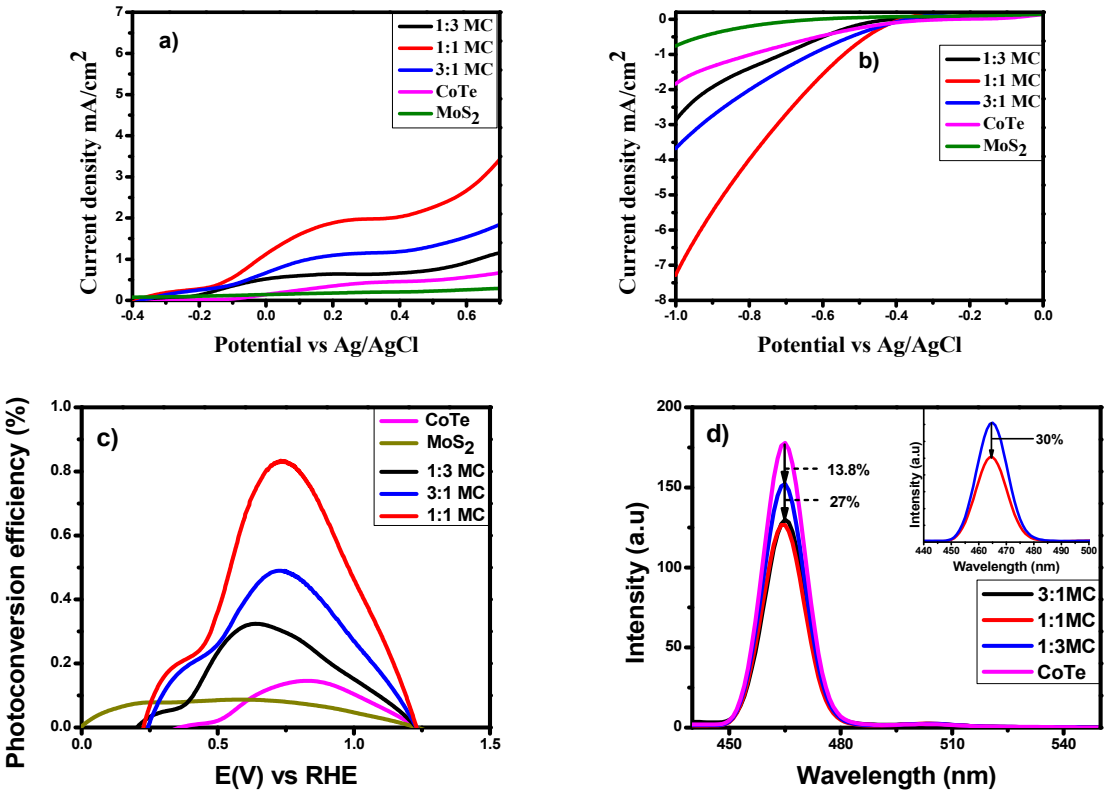

Figure 6. (**a**) I–V curves of pure MoS_2, CoTe, 1:3 MC, 1:1 MC and 3:1 MC, for oxygen evolution. (**b**) I–V curves of pure MoS_2, CoTe, 1:3 MC, 1:1 MC and 3:1 MC for hydrogen evolution. (**c**) Solar to hydrogen conversion efficiency of MoS_2, CoTe, 1:3 MC, 1:1 MC and 3:1 MC. (**d**) PL spectrum of the pure CoTe, 3:1 MC 1:1 MC and 1:3 MC.

The onset potential is an important parameter while studying photoelectrochemical properties [48]. The observed onset potentials are −0.38 V, −0.3 V and −0.1 V vs. Ag/AgCl for 1:1 MC, MoS_2 and CoTe, respectively, as shown in Figure 6a. The gradual slope increase can be attributed to jumping of the electrons from the valence band to the conduction band till the point of saturation, and then the sharp increase in photocurrent is observed. This shows efficient charge separation of electron–hole pair and transportation which results in the decrease of anodic onset potential [49]. The 1:1 MC

shows an 80 mV decrease in onset potential in comparison to pristine MoS_2. This decrease in onset potential rises to 280 mV in comparison to pristine CoTe. These results illustrate the synergistic effect of MoS_2/CoTe heterojunction development with optimum 1:1 composition for maximum light harvesting. Moreover, the flower-like template of MoS_2 provides a platform to CoTe for its efficient electron–hole pair separation and its transportation at the electrode–electrolyte interface in MoS_2/CoTe heterojunction [50]. It was also evident that MoS_2 contributes to the fast transportation of photoexcited charges as shown in the J-V characteristics curve of 1:1 MC and 3:1 MC in comparison to 1:3 MC. In another way, it is observed that pristine CoTe has poor kinetics in terms of charge transportation while, when it is mixed in proper composition in the heterojunction, it boosts the electron–hole pair charge separation and transport properties of the developed photocatalysts. A comparison of reported MoS_2-based photoanodes with the current study is given in Table 1.

Table 1. A comparison of reported MoS_2-based photoanodes with the current study.

S.No.	Heterostructures	Method	Electrolyte pH	Photocurrent Density	Ref.
1.	MoS_2/CoTe	Ultrasonication	0.5M Na_2SO_4 pH = 7	2.79 mA/cm^2	This work
2.	ZnO@MoSx	Electrodeposition	0.5 M Na_2SO_4 pH = 7	1.42 mA/cm^2	[51]
3.	$NaNbO_3$/MoS_2	Hydrothermal	0.5 M Na_2SO_4 pH = 7	3.56 mA cm^{-2}	[52]
4.	In_2Se_3/MoS_2	Ultrasonication	1 M Na_2SO_4 pH = 7	8 μA/cm^2	[53]
5.	Au-MoS_2	Stirring	0.1 M KH_2PO_4 pH = 7	790 μA/cm^2	[29]
6.	MoS_2/$BiVO_4$	Hydrothermal	1 M Na_2SO_4 pH = 7	0.63 mA/cm^2	[54]

The cathodic current also shows a good response to the hydrogen evolution at the counter electrode as shown in Figure 6b. The pure CoTe and MoS_2 exhibited a photocurrent density of −1.76 and −0.65 mA with an onset potential of −0.33 and −0.65 V vs. Ag/AgCl, respectively. The formation heterojunction changes the response of photocurrent for the composites. The 1:3 MC and 3:1 MC showed the maximum photocurrent density of −2.84 mA and −3.604 mA with an onset potential of −0.41 and −0.34 V vs. Ag/AgCl, respectively. The best results were observed with the 1:1 MC composite showing a photocurrent density of −7.21 mA with an onset potential of −0.36 V vs. Ag/AgCl. These outcomes also match with the results of anodic photocurrent response leading to a better formation of p-n heterojunction among CoTe and MoS_2.

Solar to hydrogen conversion efficiency (STH) is presented as shown in Figure 6c. A lesser onset potential means less applied bias is required to gain optimum STH [55]. The STH is calculated by using Equation (1):

$$\boldsymbol{\eta = I(1.23 - V)/P\text{in}} \quad (1)$$

where η is the STH, I is photocurrent density at the given potential, V is the applied potential vs. RHE, Pin the intensity of the irradiating light at 100 mW/cm^2 [6]. Pure MoS_2 and CoTe exhibit a maximum conversion efficiency of 0.14 and 0.08% at an applied bias of 0.82 V and 0.36 V, respectively. Heterojunction MoS_2/CoTe with 1:3 and 3:1 showed an STH efficiency of 0.325% and 0.48% at an applied bias of 0.65 V and 0.72 V vs. RHE, respectively. The highest STH efficiency was achieved with the 1:1 MC photocatalyst with 0.82% at an applied bias of 0.72 V vs. RHE. The composite heterojunction is working effectively with increased photocurrent response thereby increasing the STH efficiency. These results agree well with the J-V characteristics.

The electron–hole recombination and the efficiency of trapping the charge can be determined using the photoluminescence (PL) [56] as shown in Figure 6d. Figure 6d shows that pristine CoTe, 3:1 MC (13.8%) and 1:3 MC (27%) exhibited decrease in PL intensity as compared to 1:1 MC. It is evident that heterostructure 1:1 MC showed a 30% decrease as compared to the pure CoTe signal, so there is an effective charge transfer taking place through a successfully operating p-n junction. A facile electron transfer is taking place thus reducing the electron/hole recombination. These results are in agreement with the J-V characteristics of the photocatalysts and empowered the development of such type of heterojunctions to improve the photochemical properties of the component catalysts to integrate and deploy for efficient and smart solar cell devices and their large scale production.

Electrochemical impedance spectroscopy was employed to have a profound understanding of the charge transfer mechanism in darkness (Figure 7a) and in light (Figure 7b) under open circuit potential (OCP) conditions. The curves show two semicircles in darkness in Figure 7a. Charge transfer resistance is associated with the first semicircle at the high-frequency region and mass transfer resistance is connected to the second at the low-frequency region [57]. Whereas the inset in Figure 7a displays the high-frequency region in dark, which signifies mass transfer to be the dominant phenomenon. Figure 7b displays the OCP conditions in light and there are no semicircles observed in the high-frequency region as shown in the inset of Figure 7b. This may be due to the charge transfer as a prominent process in presence of light [58]. Typically, the reduced diameter of the semicircle shows less amount of charge transfer resistance on the electrode and electrolyte interface [59]. Hence, the recombination decreases significantly in 1:1 MC heterojunction as suggested by LSV and PL results, showing effective charge transfer as compared to pristine components of heterojunction.

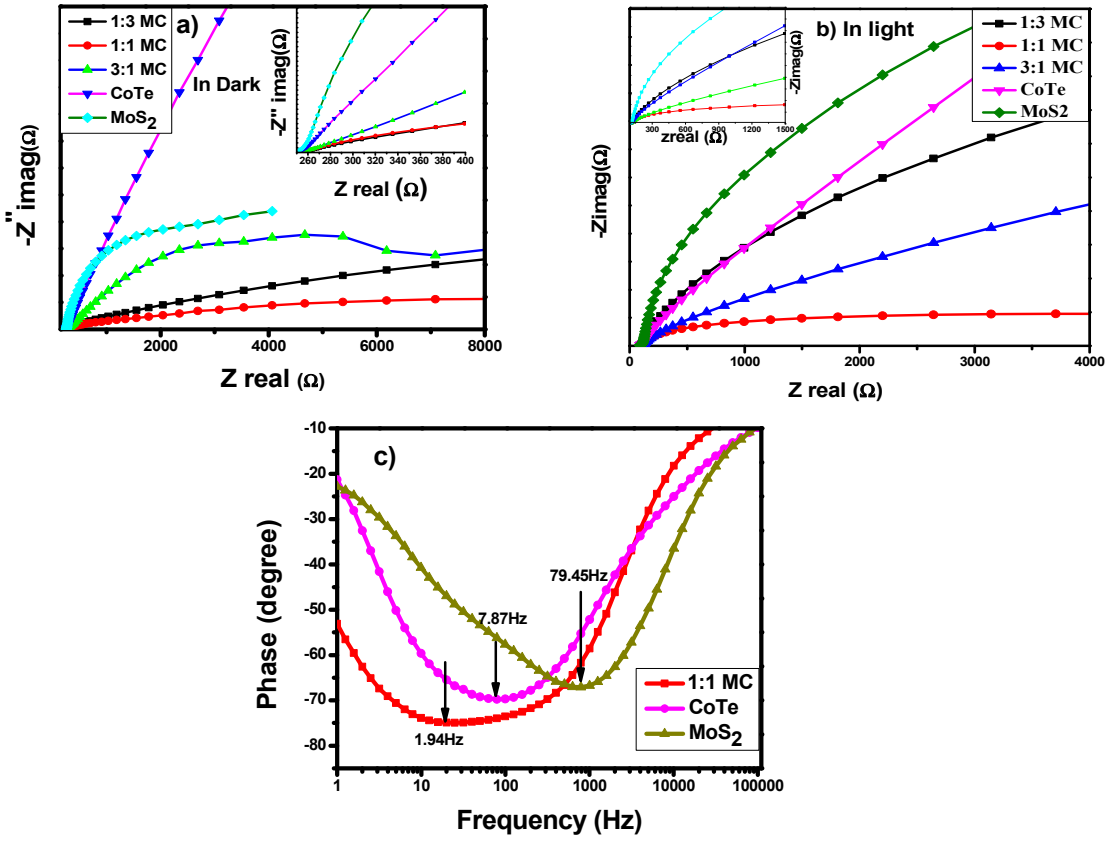

Figure 7. (**a**) Nyquist plot of the pure and composites in dark, (**b**) Nyquist plot of pure and composites in light and (**c**) Bode plot.

The Bode plot in Figure 7c shows the characteristic peak frequencies of the pure and 1:1 MC composite heterojunction. The characteristic peak frequency shifts to a lower value from MoS_2 to

CoTe to 1:1 MC, owing to the longer lifetime (1.94 Hz) of the photoexcited charges in heterojunction of 1:1 MC as compared to the pure counterparts [60]. These results are in agreement with J-V and PL studies and support the strategy of developing a potential p-n type of heterojunction with their comparable band gaps.

2.7. Mott–Schottky Plot

The Mott–Schottky plots of pristine MoS_2, CoTe, 1:3 MC, 1:1 MC and 3:1 MC heterojunctions have been obtained and presented in Figure S3 (Supplementary Material). Mott–Schottky peaks of pure MoS_2 and CoTe and the composites are shown in Figure S3a (Supplementary Material). The peaks show a trend of increasing n-character in the composites hence showing more PEC activity and formation of the p-n junction. The positive slope in Figure S3b (Supplementary Material) shows the n-type nature of MoS_2. While the CoTe showed a negative slope in Figure S3c (Supplementary Matterial) owing to the p-type nature of CoTe semiconductor. This confirms the formation of an effective p-n junction viable for photoelectrochemical water splitting. Figure S4 shows a corresponding I–t curve at a potential of −0.4 V under the chopped light illumination. The photocurrent increases immediately from OFF to ON state proving that the present system is sensitive to light illumination and efficient in the generation and separation of electron–hole pairs through p-n junction to the counter electrode for water splitting.

3. Experimental

3.1. Synthesis of MoS_2

MoS_2 was synthesized using a hydrothermal method [61]. Sodium molybdate and thiourea (1:4 mole ratio) were dissolved in water (32 mL) and placed in Teflon lined stainless steel autoclave (40 mL). Then the autoclave was retained in an oven (220 °C) for 24 h. After the benchtop cooling, the obtained black powder was washed three times with deionized water and then with ethanol followed by vacuum drying (at 70 °C) for 24 h.

3.2. Synthesis of CoTe

Cobalt telluride was synthesized using a hydrothermal route [35]. During the synthesis procedure, tellurium powder and $CoCl_2$ (1:1 mole ratio) were dissolved in 6 M KOH solution (32 mL). Hydrazine hydrate (8 mL) was added to this mixture and stirring was done for 1 h at room temperature. The mixture was transferred to a 40 mL Teflon lined autoclave. The autoclave was placed for 3 h (200 °C) in the oven. The precipitates were obtained and washed three times with deionized water and ethanol. The collected powder was dried in an oven (70 °C).

3.3. Development of MoS_2/CoTe Heterojunction Using Sonochemical Method

MoS_2/CoTe heterojunctions were developed by the sonochemical method. The heterostructures were prepared with wt. % ratios of 1:3, 1:1 and 3:1 of MoS_2 to CoTe. For a 1:1 ratio, MoS_2 (50 mg) and CoTe (50 mg) were dispersed in ethanol (25 mL) under ultrasonic shaking for 3 h. Finally, the powder was vacuum dried (80 °C) for 10 h. Other ratios were made in the same manner. These heterostructures were used for photoelectrochemical water splitting. A schematic illustration of the formation mechanism is shown in Scheme 1.

3.4. Characterization

XRD analysis was recorded on an X-ray powder diffractometer [STOE Germany] by using Cu Kα at λ = 1.54 Å. UV–vis and DRS analyses were performed on Perkin Elmer [Massachusetts, USA] Lambda 365 spectrometer. VEGA3 TESCAN [Fuveau, France] scanning electron microscope in combination with an energy-dispersive X-ray spectroscope was used to obtain images and elemental composition of the photocatalysts at an acceleration voltage of 20 KV. Photoluminescence spectra were obtained by using Perkin Elmer [Massachusetts, USA] FL 6500/8500 spectrometer. The X-ray

photoelectron spectroscopic analysis was carried out on the ESCALAB 250Xi [Massachusetts, USA] X-ray photoelectron spectrophotometer. Raman spectra were obtained using a BTC162E-532S-SYS [Newark, DE, USA] system with a 532 nm excitation wavelength.

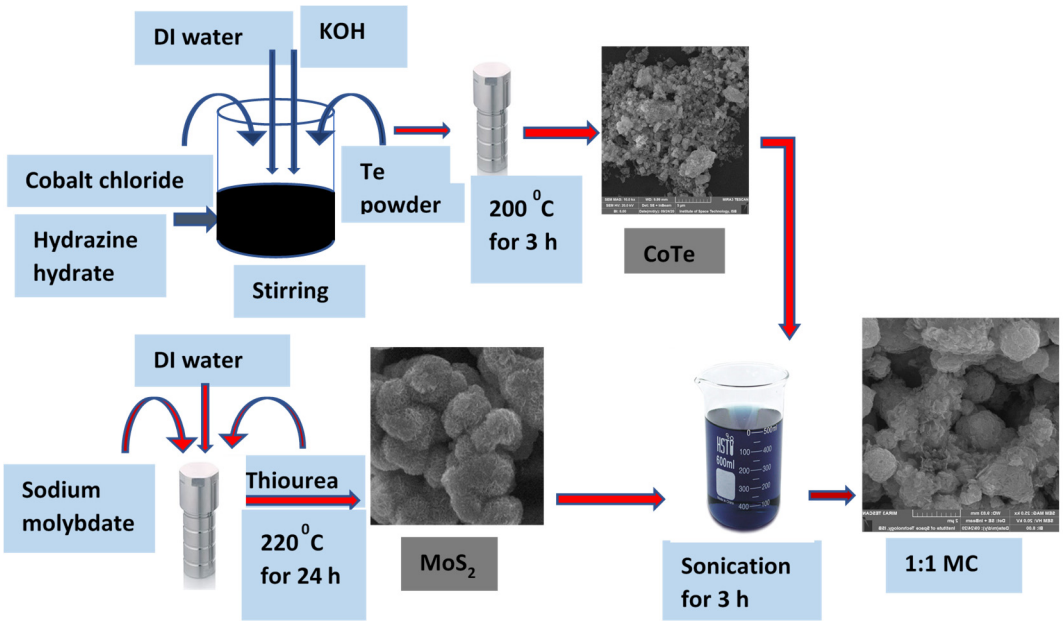

Scheme 1. Schematic illustration of MoS_2, CoTe and MoS_2/CoTe heterostructure formation.

3.5. Photoelectrochemical Measurements

Photoelectrochemical (PEC) studies were performed using a quartz cell made up of three electrode system. Platinum gauze was used as a counter electrode and Ag/AgCl as a reference electrode. FTO slides were used as a working electrode with a working area of 1 cm^2. A 0.5 M sodium sulfate solution was used as an electrolyte to maintain the stability of the working sulfide electrode. A solar simulator [Solar Light Company, Inc. Glenside PA, USA] was used to carry out studies under illumination. A 300 W Xe lamp was used with a cut off filter of $\lambda > 420$ nm for the visible light source. The incident intensity of the light was calibrated and kept at 100 mW/cm^2 of AM 1.5G using standard silicon solar cell (DyeSole). The photoelectrochemical measurements were taken on Gamry potentiostat [Philadelphia, PA, USA]. The photoelectrodes were prepared by making the sample ink. The ink was prepared by mixing 20 mg of the photocatalyst in 0.5 mL of DI water and adding 3 µL of Nafion as a binder. This mixture was ultrasonicated, to form a homogeneous ink, for 2 h. The as-prepared sample was drop casted on the FTO substrate (1 cm^2 area) and air-dried for further studies.

4. Conclusions

In the present study, a novel and effective p-n heterojunction was designed between MoS_2 and CoTe by a facile sonochemical method. MoS_2 showed a very low photocurrent response of 0.26 mA, which on the formation of an effective p-n junction with CoTe, in a 1:1 ratio, raised to 2.79 mA. This is an increase of almost 11 times as compared to the pristine MoS_2. The longer lifetime of the photoexcited charges and lessen recombination of electrons and holes was achieved and confirmed by the EIS and PL studies for 1:1 MC. Solar to hydrogen conversion efficiency also increased from 0.14% and 0.08% for MoS_2 and CoTe, respectively to 0.84% for 1:1 MC. This novel heterostructure may be a potential candidate for efficient photoelectrochemical water splitting.

Supplementary Materials: The following are available online at http://www.mdpi.com/2079-4991/10/12/2341/s1, Figure S1 (Supplementary Material) shows the SEM spectra of 3:1 MC and 1:3 MC photocatalysts, Figure S2 shows EDS spectra of MoS_2, CoTe, 3:1 MC and 1:3 MC. Figure S3 shows the Mott–Schottky plots for MoS_2, CoTe, 3:1 MC, 1:1 MC and 1:3 MC. Figure S4 shows chronoamperometric response of light on/off for 1:1 MC.

Author Contributions: Conceptualization and writing—reviewing, E.S., A.M.; supervising and writing—review, H.N., M.F.E.; methodology E.S., S.I. and S.A.B.B.; formal analysis, M.S.; writing—first draft writing E.S. All authors have read and agreed to the published version of the manuscript.

Funding: This research received no external funding.

Acknowledgments: Authors are grateful to the National University of Sciences and Technology for funding and providing all the required facilities to carry out the project.

Conflicts of Interest: The authors declare no conflict of interest.

References

1. Pan, Q.G.; Zhang, C.; Xiong, Y.J.; Mi, Q.X.; Li, D.D.; Zou, L.L.; Huang, Q.H.; Zou, Z.Q.; Yang, H. Boosting Charge Separation and Transfer by Plasmon-Enhanced $MoS_2/BiVO_4$ p-n Heterojunction Composite for Efficient Photoelectrochemical Water Splitting. *ACS Sustain. Chem. Eng.* **2018**, *6*, 6378–6387. [CrossRef]
2. Kumar, D.; Sharma, S.; Khare, N. Enhanced photoelectrochemical performance of $NaNbO_3$ nanofiber photoanodes coupled with visible light active g-C_3N_4 nanosheets for water splitting. *Nanotechnology* **2020**, *31*, 135402. [CrossRef] [PubMed]
3. Andreiadis, E.S.; Chavarot-Kerlidou, M.; Fontecave, M.; Artero, V. Artificial photosynthesis: From molecular catalysts for light-driven water splitting to photoelectrochemical cells. *Photochem. Photobiol.* **2011**, *87*, 946–964. [CrossRef]
4. Shi, X.; Cai, L.; Ma, M.; Zheng, X.; Park, J.H. General Characterization Methods for Photoelectrochemical Cells for Solar Water Splitting. *ChemSusChem* **2015**, *8*, 3192–3203. [CrossRef] [PubMed]
5. Osterloh, F.E. Inorganic nanostructures for photoelectrochemical and photocatalytic water splitting. *Chem. Soc. Rev.* **2013**, *42*, 2294–2320. [CrossRef]
6. Murphy, A.; Barnes, P.; Randeniya, L.; Plumb, I.; Grey, I.; Horne, M.; Glasscock, J. Efficiency of solar water splitting using semiconductor electrodes. *Int. J. Hydrogen Energy* **2006**, *31*, 1999–2017. [CrossRef]
7. Liao, J.; Sa, B.; Zhou, J.; Ahuja, R.; Sun, Z. Design of High-Efficiency Visible-Light Photocatalysts for Water Splitting: MoS_2/AlN(GaN) Heterostructures. *J. Phys. Chem. C* **2014**, *118*, 17594–17599. [CrossRef]
8. Li, M.; Chen, J.-S.; Routh, P.K.; Zahl, P.; Nam, C.-Y.; Cotlet, M. Distinct Optoelectronic Signatures for Charge Transfer and Energy Transfer in Quantum Dot-MoS_2 Hybrid Photodetectors Revealed by Photocurrent Imaging Microscopy. *Adv. Funct. Mater.* **2018**, *28*, 1707558. [CrossRef]
9. Kang, Z.; Yan, X.; Wang, Y.; Bai, Z.; Liu, Y.; Zhang, Z.; Lin, P.; Zhang, X.; Yuan, H.; Zhang, X.; et al. Electronic structure engineering of Cu_2O film/ZnO nanorods array all-oxide p-n heterostructure for enhanced photoelectrochemical property and self-powered biosensing application. *Sci. Rep.* **2015**, *5*, 7882. [CrossRef]
10. Liu, Y.; Yu, Y.-X.; Zhang, W.-D. MoS_2/CdS Heterojunction with High Photoelectrochemical Activity for H2Evolution under Visible Light: The Role of MoS_2. *J. Phys. Chem. C* **2013**, *117*, 12949–12957. [CrossRef]
11. Koo, B.; Shin, G.H.; Park, H.; Kim, H.; Choi, S.-Y. Vertical-tunneling field-effect transistor based on $MoTe_2/MoS_2$ 2D–2D heterojunction. *J. Phys. D Appl. Phys.* **2018**, *51*, 475101. [CrossRef]
12. Nardi, M.V.; Timpel, M.; Ligorio, G.; Zorn Morales, N.; Chiappini, A.; Toccoli, T.; Verucchi, R.; Ceccato, R.; Pasquali, L.; List-Kratochvil, E.J.W.; et al. Versatile and Scalable Strategy To Grow Sol-Gel Derived 2H-MoS_2 Thin Films with Superior Electronic Properties: A Memristive Case. *ACS Appl. Mater. Interfaces* **2018**, *10*, 34392–34400. [CrossRef] [PubMed]
13. Wang, P.; Yue, W.; Lu, Z.; Zhang, G.; Zhu, L. Friction and wear properties of MoS_2-based coatings sliding against Cu and Al under electric current. *Tribol. Int.* **2018**, *127*, 379–388. [CrossRef]
14. Sinha, A.; Dhanjai; Tan, B.; Huang, Y.; Zhao, H.; Dang, X.; Chen, J.; Jain, R. MoS_2 nanostructures for electrochemical sensing of multidisciplinary targets: A review. *TrAC Trends Anal. Chem.* **2018**, *102*, 75–90. [CrossRef]
15. Verdier, P.; Vasilevskiy, D.; Turenne, S.; Masut, R.A. Microstructure and Thermoelectric Properties of Hot Extruded Sb-Doped Mg2Si Using MoS_2 Nano-particles as Lubricant. *J. Electron. Mater.* **2018**, *47*, 6833–6841. [CrossRef]

16. Jian, W.; Cheng, X.; Huang, Y.; You, Y.; Zhou, R.; Sun, T.; Xu, J. Arrays of ZnO/MoS_2 nanocables and MoS_2 nanotubes with phase engineering for bifunctional photoelectrochemical and electrochemical water splitting. *Chem. Eng. J.* **2017**, *328*, 474–483. [CrossRef]
17. Velicky, M.; Bissett, M.A.; Woods, C.R.; Toth, P.S.; Georgiou, T.; Kinloch, I.A.; Novoselov, K.S.; Dryfe, R.A. Photoelectrochemistry of Pristine Mono- and Few-Layer MoS_2. *Nano Lett.* **2016**, *16*, 2023–2032. [CrossRef]
18. Ge, L.; Han, C.; Xiao, X.; Guo, L. Synthesis and characterization of composite visible light active photocatalysts MoS_2–g-C_3N_4 with enhanced hydrogen evolution activity. *Int. J. Hydrogen Energy* **2013**, *38*, 6960–6969. [CrossRef]
19. Lu, X.; Jin, Y.; Zhang, X.; Xu, G.; Wang, D.; Lv, J.; Zheng, Z.; Wu, Y. Controllable synthesis of graphitic C_3N_4/ultrathin MoS_2 nanosheet hybrid nanostructures with enhanced photocatalytic performance. *Dalton Trans.* **2016**, *45*, 15406–15414. [CrossRef]
20. Yuan, X.; Wang, H.; Wang, J.; Zeng, G.; Chen, X.; Wu, Z.; Jiang, L.; Xiong, T.; Zhang, J.; Wang, H. Near-infrared-driven Cr(vi) reduction in aqueous solution based on a MoS_2/Sb_2S_3 photocatalyst. *Catal. Sci. Technol.* **2018**, *8*, 1545–1554. [CrossRef]
21. Pradhan, G.; Sharma, A.K. Anomalous Raman and photoluminescence blue shift in mono- and a few layered pulsed laser deposited MoS_2 thin films. *Mater. Res. Bull.* **2018**, *102*, 406–411. [CrossRef]
22. Chen, T.; Hao, G.; Kou, L.; Wang, C.; Zhong, J. Controllable epitaxial growth of $MoSe_2$-MoS_2 lateral heterostructures with tunable electrostatic properties. *Nanotechnology* **2018**, *29*, 484003. [CrossRef] [PubMed]
23. Zhang, W.; Zhang, P.; Su, Z.; Wei, G. Synthesis and sensor applications of MoS_2-based nanocomposites. *Nanoscale* **2015**, *7*, 18364–18378. [CrossRef]
24. Sharma, S.; Kumar, A.; Singh, N.; Kaur, D. Excellent room temperature ammonia gas sensing properties of n-MoS_2/p-CuO heterojunction nanoworms. *Sens. Actuators B Chem.* **2018**, *275*, 499–507. [CrossRef]
25. Zhang, Y.; Zou, H.; Peng, J.; Duan, Z.; Ma, M.; Xin, X.; Li, W.; Zheng, X. Enhanced humidity sensing properties of $SmFeO_3$-modified MoS_2 nanocomposites based on the synergistic effect. *Sens. Actuators B Chem.* **2018**, *272*, 459–467. [CrossRef]
26. Lee, H.S.; Ahn, J.; Shim, W.; Im, S.; Hwang, D.K. 2D WSe_2/MoS_2 van der Waals heterojunction photodiode for visible-near infrared broadband detection. *Appl. Phys. Lett.* **2018**, *113*, 163102. [CrossRef]
27. Hossain, M.A.; Merzougui, B.A.; Alharbi, F.H.; Tabet, N. Electrochemical deposition of bulk MoS_2 thin films for photovoltaic applications. *Solar Energy Mater. Solar Cells* **2018**, *186*, 165–174. [CrossRef]
28. Zhang, J.; Lang, X.Y.; Zhu, Y.F.; Jiang, Q. Strain tuned InSe/MoS_2 bilayer van der Waals heterostructures for photovoltaics or photocatalysis. *Phys. Chem. Chem. Phys.* **2018**, *20*, 17574–17582. [CrossRef]
29. Yin, Z.; Chen, B.; Bosman, M.; Cao, X.; Chen, J.; Zheng, B.; Zhang, H. Au nanoparticle-modified MoS_2 nanosheet-based photoelectrochemical cells for water splitting. *Small* **2014**, *10*, 3537–3543. [CrossRef]
30. Chakrabarty, S.; Mukherjee, A.; Basu, S. RGO-MoS_2 Supported $NiCo_2O_4$ Catalyst toward Solar Water Splitting and Dye Degradation. *ACS Sustain. Chem. Eng.* **2018**, *6*, 5238–5247. [CrossRef]
31. Ghosh, D.; Devi, P.; Kumar, P. Modified p-GaN Microwells with Vertically Aligned 2D-MoS_2 for Enhanced Photoelectrochemical Water Splitting. *ACS Appl. Mater. Interfaces* **2020**, *12*, 13797–13804. [CrossRef] [PubMed]
32. Sheng, W.H.; Tian, Y.Y.; Song, Y.; Ji, J.; Wang, F. Phase controlled synthesis and the phase dependent photo-and electrocatalysis of CdS@$CoMo_2S_4$/MoS_2 catalyst for HER. *Int. J. Hydrogen Energy* **2019**, *44*, 19890–19899. [CrossRef]
33. Chen, X.; Zhang, J.; Zeng, J.H.; Shi, Y.X.; Lin, S.Y.; Huang, G.Z.; Wang, H.B.; Kong, Z.; Xi, J.H.; Ji, Z.G. MnS coupled with ultrathin MoS_2 nanolayers as heterojunction photocatalyst for high photocatalytic and photoelectrochemical activities. *J. Alloys Compd.* **2019**, *771*, 364–372. [CrossRef]
34. Lu, T.H.; Chen, C.J.; Basu, M.; Ma, C.G.; Liu, R.S. The $CoTe_2$ nanostructure: An efficient and robust catalyst for hydrogen evolution. *Chem. Commun.* **2015**, *51*, 17012–17015. [CrossRef]
35. Khan, M.S.; Ashiq, M.N.; Ehsan, M.F.; He, T.; Ijaz, S. Controlled synthesis of cobalt telluride superstructures for the visible light photo-conversion of carbon dioxide into methane. *Appl. Catal. A Gen.* **2014**, *487*, 202–209. [CrossRef]
36. Bazri, B.; Lin, Y.C.; Lu, T.H.; Chen, C.J.; Kowsari, E.; Hu, S.F.; Liu, R.S. A heteroelectrode structure for solar water splitting: Integrated cobalt ditelluride across a TiO_2-passivated silicon microwire array. *Catal. Sci. Technol.* **2017**, *7*, 1488–1496. [CrossRef]
37. Aguilera, E.N.; Jerez, L.M.B.; Alonso, J.L. Electrochemical metallation with Ni(II) and Al(III) of 5,10,15,20-tetrakis(p-hydroxyphenyl)porphyrin: Effect of ultrasound. *Electrochim. Acta* **2013**, *98*, 82–87. [CrossRef]

38. Wang, X.; Xiong, W.; Li, X.; Zhao, Q.; Fan, S.; Zhang, M.; Mu, J.; Chen, A. Fabrication of MoS_2@g-C_3N_4 core-shell nanospheres for visible light photocatalytic degradation of toluene. *J. Nanopart Res.* **2018**, *20*, 243. [CrossRef]
39. Zhang, X.; Suo, H.; Zhang, R.; Niu, S.; Zhao, X.q.; Zheng, J.; Guo, C. Photocatalytic activity of 3D flower-like MoS_2 hemispheres. *Mater. Res. Bull.* **2018**, *100*, 249–253. [CrossRef]
40. Vangelista, S.; Cinquanta, E.; Martella, C.; Alia, M.; Longo, M.; Lamperti, A.; Mantovan, R.; Basset, F.B.; Pezzoli, F.; Molle, A. Towards a uniform and large-scale deposition of MoS_2 nanosheets via sulfurization of ultra-thin Mo-based solid films. *Nanotechnology* **2016**, *27*, 175703. [CrossRef]
41. Wang, C.; Lin, H.; Xu, Z.; Cheng, H.; Zhang, C. One-step hydrothermal synthesis of flowerlike MoS_2/CdS heterostructures for enhanced visible-light photocatalytic activities. *RSC Adv.* **2015**, *5*, 15621–15626. [CrossRef]
42. Newbury, D.E.; Ritchie, N.W. Performing elemental microanalysis with high accuracy and high precision by scanning electron microscopy/silicon drift detector energy-dispersive X-ray spectrometry (SEM/SDD-EDS). *J. Mater. Sci.* **2015**, *50*, 493–518. [CrossRef] [PubMed]
43. Cao, Y.; Gao, Q.; Li, Q.; Jing, X.; Wang, S.; Wang, W. Synthesis of 3D porous MoS_2/g-C_3N_4 heterojunction as a high efficiency photocatalyst for boosting H2 evolution activity. *RSC Adv.* **2017**, *7*, 40727–40733. [CrossRef]
44. Shi, L.; He, Z.; Liu, S. MoS_2 quantum dots embedded in g-C_3N_4 frameworks: A hybrid 0D-2D heterojunction as an efficient visible-light driven photocatalyst. *Appl. Surf. Sci.* **2018**, *457*, 30–40. [CrossRef]
45. Ji, W.; Shen, R.; Yang, R.; Yu, G.; Guo, X.; Peng, L.; Ding, W. Partially nitrided molybdenum trioxide with promoted performance as an anode material for lithium-ion batteries. *J. Mater. Chem. A* **2014**, *2*, 699–704. [CrossRef]
46. Manikandan, M.; Subramani, K.; Sathish, M.; Dhanuskodi, S. Hydrothermal synthesis of cobalt telluride nanorods for a high performance hybrid asymmetric supercapacitor. *RSC Adv.* **2020**, *10*, 13632–13641. [CrossRef]
47. Ehsan, M.F.; Qudoos, S.; Ahmad, Z.; Hamid, S.; Arfan, M.; Zia, A.; Umbreen, K.; Ashiq, M.N.; Tyagi, D. ZnTe/ZnSe heterostructures: In-situ synthesis, characterization and photocatalytic activity for Congo Red degradation. *SN Appl. Sci.* **2019**, *1*, 197. [CrossRef]
48. Wu, H.; Ren, F.; Xing, Z.; Zheng, X.; Wu, L.; Jiang, C. Cathodic shift of onset potential for water oxidation of WO_3 photoanode by Zr^+ ions implantation. *J. Appl. Phys.* **2017**, *121*, 085305. [CrossRef]
49. Bai, S.; Yang, X.; Liu, C.; Xiang, X.; Luo, R.; He, J.; Chen, A. An Integrating Photoanode of WO_3/Fe_2O_3 Heterojunction Decorated with NiFe-LDH to Improve PEC Water Splitting Efficiency. *ACS Sustain. Chem. Eng.* **2018**, *6*, 12906–12913. [CrossRef]
50. Theerthagiri, J.; Senthil, R.A.; Senthilkumar, B.; Reddy Polu, A.; Madhavan, J.; Ashokkumar, M. Recent advances in MoS_2 nanostructured materials for energy and environmental applications—A review. *J. Solid State Chem.* **2017**, *252*, 43–71. [CrossRef]
51. Sharma, M.D.; Mahala, C.; Basu, M. Sensitization of vertically grown ZnO 2D thin sheets by MoSx for efficient charge separation process towards photoelectrochemical water splitting reaction. *Int. J. Hydrogen Energy* **2020**, *45*, 12272–12282. [CrossRef]
52. Kumar, S.; Malik, T.; Sharma, D.; Ganguli, A.K. $NaNbO_3$/MoS_2 and $NaNbO_3$/$BiVO_4$ Core–Shell Nanostructures for Photoelectrochemical Hydrogen Generation. *ACS Appl. Nano Mater.* **2019**, *2*, 2651–2662. [CrossRef]
53. Jiang, Y.; Wang, Q.; Han, L.; Zhang, X.; Jiang, L.; Wu, Z.; Lai, Y.; Wang, D.; Liu, F. Construction of In_2Se_3/MoS_2 heterojunction as photoanode toward efficient photoelectrochemical water splitting. *Chem. Eng. J.* **2019**, *358*, 752–758. [CrossRef]
54. Nan, F.; Cai, T.; Ju, S.; Fang, L. Enhanced photoelectrochemical water splitting of $BiVO_4$ photonic crystal photoanode by decorating with MoS_2 nanosheets. *Appl. Phys. Lett.* **2018**, *112*, 173902. [CrossRef]
55. Yang, X.; Wolcott, A.; Wang, G.; Sobo, A.; Fitzmorris, R.C.; Qian, F.; Zhang, J.Z.; Li, Y. Nitrogen-doped ZnO nanowire arrays for photoelectrochemical water splitting. *Nano Lett.* **2009**, *9*, 2331–2336. [CrossRef]
56. Jiang, L.; Zhu, Y.-J.; Cui, J.-B. Nanostructures of Metal Tellurides (PbTe, CdTe, $CoTe_2$, Bi_2Te_3, and Cu_7Te_4) with Various Morphologies: A General Solvothermal Synthesis and Optical Properties. *Eur. J. Inorg. Chem.* **2010**, *2010*, 3005–3011. [CrossRef]
57. Liu, Q.; Ding, D.; Ning, C.; Wang, X. Black Ni-doped TiO_2 photoanodes for high-efficiency photoelectrochemical water-splitting. *Int. J. Hydrogen Energy* **2015**, *40*, 2107–2114. [CrossRef]
58. Xu, X.; Zhou, G.; Dong, X.; Hu, J. Interface Band Engineering Charge Transfer for 3D MoS_2 Photoanode to Boost Photoelectrochemical Water Splitting. *ACS Sustain. Chem. Eng.* **2017**, *5*, 3829–3836. [CrossRef]

59. Hou, Y.; Zuo, F.; Dagg, A.; Feng, P. A three-dimensional branched cobalt-doped alpha-Fe_2O_3 nanorod/$MgFe_2O_4$ heterojunction array as a flexible photoanode for efficient photoelectrochemical water oxidation. *Angew. Chem.* **2013**, *52*, 1248–1252. [CrossRef] [PubMed]
60. Zhou, M.; Bao, J.; Xu, Y.; Zhang, J.; Xie, J.; Guan, M.; Wang, C.; Wen, L.; Lei, Y.; Xie, Y. Photoelectrodes based upon Mo:$BiVO_4$ inverse opals for photoelectrochemical water splitting. *ACS Nano* **2014**, *8*, 7088–7098. [CrossRef] [PubMed]
61. Miao, H.; Hu, X.; Sun, Q.; Hao, Y.; Wu, H.; Zhang, D.; Bai, J.; Liu, E.; Fan, J.; Hou, X. Hydrothermal synthesis of MoS_2 nanosheets films: Microstructure and formation mechanism research. *Mater. Lett.* **2016**, *166*, 121–124. [CrossRef]